



Synthesis of non-noble metal nickel doped sulfide solid solution for improved photocatalytic performance

Houde She^a, Yidong Sun^a, Shiping Li^b, Jingwei Huang^a, Lei Wang^a, Gangqiang Zhu^{b,*}, Qizhao Wang^{a,*}

^a College of Chemistry and Chemical Engineering, Research Center of Gansu Military and Civilian Integration Advanced Structural Materials, Northwest Normal University, Lanzhou, 730070, China

^b School of Physics and Information Technology, Shaanxi Normal University, Xi'an, 710062, China

ARTICLE INFO

Keywords:

Metal doping
Photocatalyst
Hydrogen evolution
Selective oxidation

ABSTRACT

Bimetallic Sulfides, a series of versatile catalysts, are still hampered from putting into practical application due to the issue of the recombination of photogenerated charges. In this work, in order to enhance the light harvesting ability as well as ameliorate the separation and transportation of photo-induced charges at the same time, Ni ion was adopted to modify $\text{Zn}_{0.5}\text{Cd}_{0.5}\text{S}$ catalyst. The subsequent photocatalytic water splitting tests showed that the H_2 evolution rate over Ni doped $\text{Zn}_{0.5}\text{Cd}_{0.5}\text{S}$ was 6 times higher than that achieved on the pristine $\text{Zn}_{0.5}\text{Cd}_{0.5}\text{S}$, indicating a significant enhancement in catalytic activity. Furthermore, the selective oxidation of benzyl alcohol was also performed by the as-prepared catalysts under visible light irradiation. When 1% Ni ions were doped in $\text{Zn}_{0.5}\text{Cd}_{0.5}\text{S}$ solid solution, the yield of product benzaldehyde was increased from 70% to 92%. The photoelectrochemical test suggests that the improved photocatalytic performance is presumably ascribed to the efficient separation of photo-generated carriers. Additionally, DOS calculation confirms the contribution of the improved light harvesting ability of Ni-doped $\text{Zn}_{0.5}\text{Cd}_{0.5}\text{S}$ in the photocatalytic reaction. In all, this work presents that doping Ni into ZnS/CdS solid solution is a very useful technique to improve photocatalytic activity for two typical photocatalytic reactions-the H_2 evolution and alcohol selective oxidation reaction.

1. Introduction

Recently, energy shortage and environment pollution caused by undue exploitation of fossil fuels have aroused increasing concerns about the future of human, which stimulates great progress in the development of green renewable energy. Hydrogen, a clean and renewable energy source, is regarded as one of the most promising solutions to this dilemma. Since the 1970s, when Honda and Fujishima applied TiO_2 to photocatalysis for transmuting water into H_2 and O_2 [1,2], numerous researchers have increasingly focused on studying the water splitting process conducted by metal-based nanoparticles [3–10]. However, many photocatalysts only absorb UV light that constitutes merely 4% of the total sunlight, severely restricting the industrial application of water splitting technique. In this case, developing visible-light responding photocatalysts becomes an efficacious method to make effective use of solar energy in photocatalysis [11–13]. Among those well designed and prepared photocatalysts [14–20], metal sulfides like CdS -based materials are potential candidates due to their tunable band

gaps and low cost [21–29]. For example, the conduction band of $\text{Zn}_x\text{Cd}_{1-x}\text{S}$ can be regulated through correspondingly adjusting the ratio between spiked Zn and Cd in the composites [30,31]. According to previous reports [32–37], $\text{Cd}_x\text{Zn}_{1-x}\text{S}$ exhibits excellent performance in water splitting process under visible light irradiation whilst maintaining consistent chemical stability. Yet the application of $\text{Cd}_x\text{Zn}_{1-x}\text{S}$ is still limited because it suffers strong electron-hole recombination. In order to reduce the recombination of photo-induced carriers, the method of doping metal ions differing from the major metal in the photocatalysts has been adopted [38–42]. For example, in case of Cu^{2+} doped $\text{Zn}_x\text{Cd}_{1-x}\text{S}$, the Cu^{2+} dopant can capture electron, thus decreasing electron-hole recombination and increasing the efficiency of water splitting under visible light [38]. As Zhang and Liu demonstrated [39,40], Cu^{2+} is able to enhance the photocatalytic activities by forming dopant impurity levels for greater charge separation. Besides, doping Sr [41] and La [42] can improve the photocatalytic activities with an optimized hydrogen production of 18,000 $\mu\text{mol}/\text{h}/\text{g}$, which was achieved via the formation of a novel energy level in the band

* Corresponding authors.

E-mail addresses: zgq2006@snmu.edu.cn (G. Zhu), wangqizhao@163.com (Q. Wang).

<https://doi.org/10.1016/j.apcatb.2019.01.002>

Received 25 September 2018; Received in revised form 22 December 2018; Accepted 1 January 2019

Available online 02 January 2019

0926-3373/ © 2019 Elsevier B.V. All rights reserved.

structure [43–45].

Based on these studies mentioned above, in this work, Ni^{2+} doped $\text{Zn}_x\text{Cd}_{1-x}\text{S}$ was synthesized via a solvothermal method and further testified to by its photocatalytic activities in water splitting as well as benzyl alcohol selective oxidation. Compared with pure $\text{Zn}_{0.5}\text{Cd}_{0.5}\text{S}$ (ZCS), the water splitting photocatalyzed by Ni^{2+} doped $\text{Zn}_{0.5}\text{Cd}_{0.5}\text{S}$ (Ni-ZCS(x %)) shows an optimal H_2 evolution rate of 31,000 $\mu\text{mol}/\text{h/g}$, which is 6 times greater than using ZCS alone. In addition, ZCS also present notable activities in selective catalytic oxidation of benzyl alcohols, as 92% for the yield, 95% for the conversion and 98% for the selectivity under visible light irradiation at 1 atm gas pressure.

2. Experimental section

2.1. Materials

$\text{Ni}(\text{CH}_3\text{COO})_2 \cdot 4\text{H}_2\text{O}$, $\text{Cd}(\text{NO}_3)_2 \cdot 4\text{H}_2\text{O}$, $\text{Zn}(\text{NO}_3)_2 \cdot 6\text{H}_2\text{O}$, $(\text{NH}_4)_2\text{S}$, CH_4O , $\text{C}_2\text{H}_6\text{O}$ are purchase from Sinopharm Chemical Reagent Co., Ltd., China. $\text{C}_7\text{H}_5\text{F}_3$ (BTF), P-nitrobenzyl alcohol ($\text{C}_7\text{H}_7\text{NO}_3$), p-methoxybenzyl alcohol ($\text{C}_8\text{H}_{10}\text{O}_2$), p-chlorobenzyl alcohol ($\text{C}_7\text{H}_7\text{ClO}$) are purchase from Aladdin Chemical Reagent Co., Ltd., China. Benzylalcohol ($\text{C}_7\text{H}_8\text{O}$) is purchase from Alfa Aesar Chemical Co., Ltd., China. All reagents are analytical grade and used without further purification.

2.2. Preparation of Ni-ZCS(x %)

Ni-ZCS(6%) was synthesized by a solvothermal method using ethanol as the solvent. In a typical synthesis, 2.2 mmol of $\text{Zn}(\text{NO}_3)_2 \cdot 6\text{H}_2\text{O}$, 2.5 mmol of $\text{Cd}(\text{NO}_3)_2 \cdot 4\text{H}_2\text{O}$, and 0.3 mmol of $\text{Ni}(\text{CH}_3\text{COO})_2 \cdot 4\text{H}_2\text{O}$ were dissolved in 20 ml ethanol. Then, 7.5 mmol of $(\text{NH}_4)_2\text{S}$ was dripped into the mixed solution and kept stirring for 20 min before it was transferred into a Teflon liner together with 50 ml of alcohol. The liner was sealed by a stainless steel autoclave and heated at 180 °C for 24 h in an oven. After that, the products were cleaned using distilled water and ethanol alternately and then dried in an oven at 80 °C. For the synthesis of Ni-ZCS (x %), the procedure was the same as that of the Ni-ZCS(6%) except that different amount of $\text{Ni}(\text{CH}_3\text{COO})_2 \cdot 4\text{H}_2\text{O}$ was added.

2.3. Characterization

Transmission electron microscopy (TEM) images were obtained from a TECNAI G2 F20, America FEI. The morphologies of the products were obtained by field emission scanning electron microscope (FE-SEM, Ultra Plus, Carl Zeiss), X-ray diffraction (XRD) patterns were acquired using a Bruker D8 equipped with $\text{Cu K}\alpha$ radiation. UV–vis diffuse reflectance spectra were measured by a PuXinTU-1901 spectrophotometer. X-ray photoelectron spectroscopic (XPS) characterizations were performed on a PHI5702 photoelectron spectrometer. The photoelectrochemical (PEC) performances of photoanodes were acquired by a three-electrode system (CHI-660D Co., Shanghai, China) under a LED lamp ($\lambda > 420\text{ nm}$, CEL-LED 100) illumination. The photoluminescence spectra were obtained at room temperature on a Hitachi FL - 4500 Fluorescence Spectrophotometer. The electronspin resonance (ESR) signals of radicals spin-trapped by spin-trapreagent DMPO (Sigma Chemical Co.) were examined on a ESR spectrometer (JES-FA 200, Bruker).

2.4. Photocatalytic test

The photocatalytic activities of the Ni-ZCS(x%) were carried out in a reactor. In each test, 0.1 g of the photocatalyst powder was dispersed in 100 ml of 0.5 M $\text{Na}_2\text{S}_9\text{H}_2\text{O}$ and 0.5 M Na_2SO_3 aqueous solution. The mixture was then under irradiation of visible light using a 300 W Xe lamp, which is combined with a 420 nm cut-off filter (0.1 M NaNO_2

aqueous solution). A gas chromatography (GC 9560, China) was used to separate evolved H_2 once an hour during a test cycle. The amount of H_2 was measured by a thermal conductivity detector (Ar carrier).

2.5. Electrode preparation

The photoelectrochemical (PEC) performances of photoanodes were acquired by a three-electrode system under a LED lamp ($\lambda > 420\text{ nm}$, CEL-LED 100) illumination. A Pt wire and Ag/AgCl were used as counter electrode and reference electrode, respectively. The working electrodes were made on the fluoride-tin oxide (FTO) conductor glasses. The samples (10 mg) were homogeneously dispersed in anhydrous ethanol and ultrasound for 20 min before they were slowly dripped on FTO glasses. The working electrodes were dried under the infrared lamp irradiation for 30 min. The electrolyte was 0.5 M Na_2SO_4 ($\text{pH} = 7.5$) aqueous solution in a quartz ware. 0.5 V of the bias voltage was used for photoelectrochemical testing. The measured potential vs. Ag/AgCl was converted to reversible hydrogen electrode (RHE) scale using the Nernst equation: $E_{\text{RHE}} = E_{\text{Ag/AgCl}} + 0.197 + 0.059\text{ pH}$. Illumination through the back - side of FTO was used with an illumination area of about 1.0 cm^2 [46,47].

2.6. Computational method

First-principle calculation is performed with Cambridge Sequential Total Energy Package (CASTEP). The geometry optimization is carried out by using the Broyden Fletcher Goldfrab Shanno (BFGS) routine. The electron-electron exchange correlation interaction is considered with generalized gradient approximation with Perdew-Burke-Ernzerhof for solid (GGA-PBESol). The electronic wave functions are expanded in a plane wave set with energy cutoff of 380 eV. For the calculation of structural and electronic properties, $3 \times 3 \times 4$ Monkhorst-pack mesh grid is employed. All the atoms are relaxed to their equilibrium positions when the successive energy change on each atom is less than 5.0×10^{-6} eV, the force applied on each atom is less than 0.01 eV/Å and the stress is less than 0.02 GPa, the displacement is less than 5.0×10^{-4} Å. The atomic electronic configuration considered is $\text{Ni } 3\text{p}^6 3\text{d}^8 4\text{s}^2$, $\text{Zn } 3\text{d}^{10} 4\text{s}^2$, $\text{Cd } 4\text{d}^{10} 5\text{s}^2$, $\text{S } 3\text{s}^2 3\text{p}^4$ [48–50].

3. Results and discussion

The SEM images of the as-prepared samples are shown in Fig. 1(a). It can be seen that the Ni-ZCS(6%) synthesized by the solvothermal method are relatively evenly dispersed nano-particles (NPs) with a small size of 50 nm. The small-particles catalysts with uniform dispersion tend to play better catalytic performance. Fig. 1(b, c) and (d) shows the typical TEM and HRTEM of Ni-ZCS(6%). The average size of the nano-particles is about 50 nm. Fig. 1(d) implies the interplanar spacings of the sample Ni-ZCS(6%) is about 3.2 Å, which agrees well with the d value of (111) plane (shown in Fig. 3) calculated from Bragg equation.

Elemental mapping and TEM analyses were carried out on the as-prepared samples to prove the successful synthesis of Ni-ZCS(x %). The signals of Ni, Zn, Cd, S elements can be observed in Fig. 2, indicating that Ni was successfully doped in the ZCS solid solution.

The X-ray diffraction (XRD) patterns of ZCS and Ni-ZCS(1–7%) are shown in Fig. 3. The (111), (200), (220) and (311) crystal plane of Ni-ZCS(1–7%) can be clearly seen in Fig. 3. As compared with pristine ZCS, the peaks of Ni-ZCS(1–7%) show no obvious shift, and the intensity of the diffraction peaks were virtually unchanged as well, indicating that the crystal structure of the composite catalyst maintain consistent with pure ZCS after doping Ni. The average particle size is calculated by Debye-Scherrer's formula, giving the result of 13.6 nm. All peaks of ZCS samples lie between the standard situation of cubic ZnS (JCPDS: No. 05-0566) and cubic CdS (JCPDS: No. 10-0454) due to the formation of ZCS solid solution (Fig. S2).

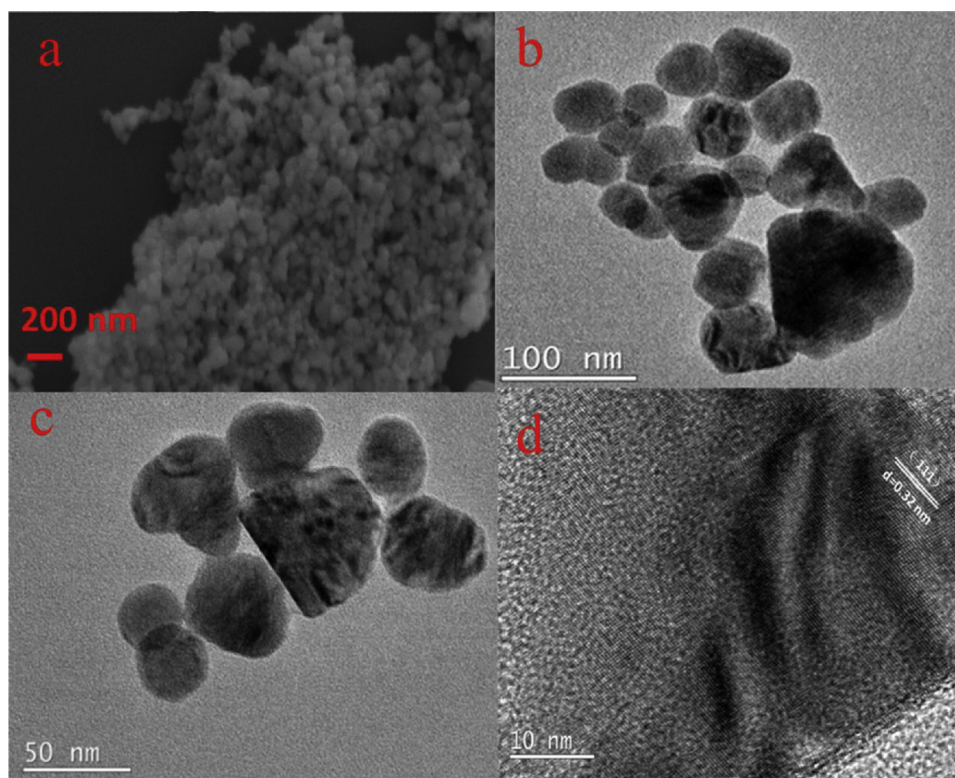


Fig. 1. (a) The typical SEM images of Ni-ZCS(6%), TEM images (b, c), and HRTEM images (d) of Ni-ZCS (6%).

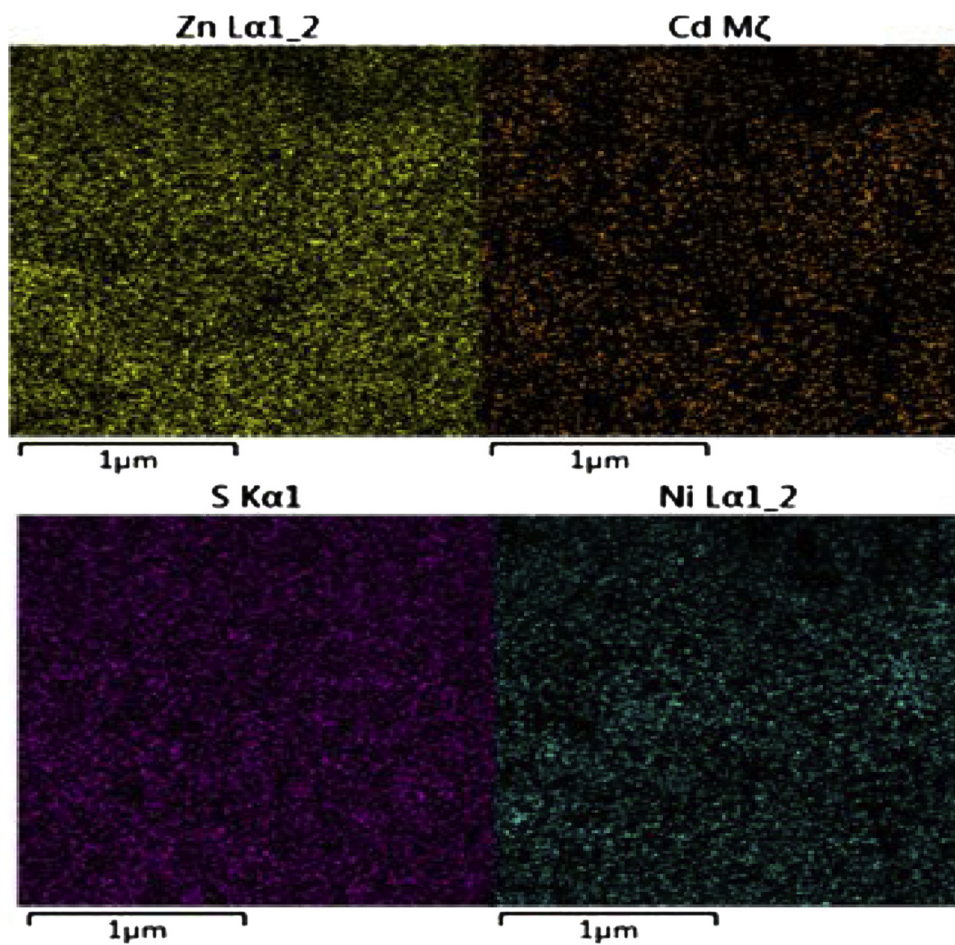


Fig. 2. Elemental mapping images of Ni-ZCS(6%).

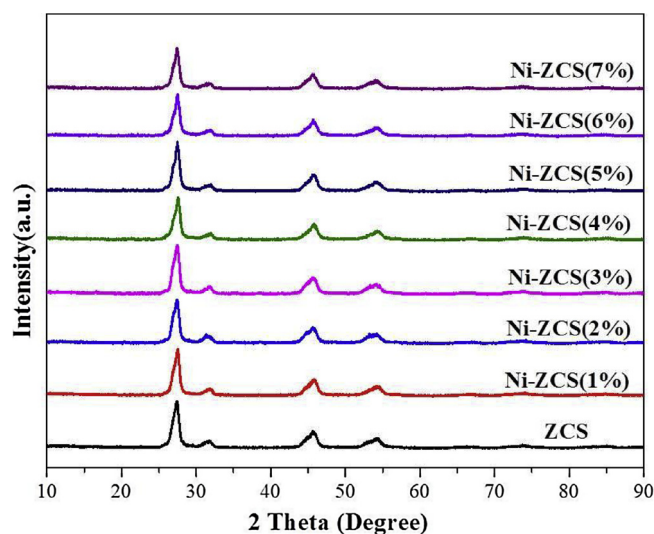


Fig. 3. The XRD patterns of ZCS and Ni-ZCS (x%).

$$D = \frac{k\lambda}{\beta \cos \theta}$$

The XPS analysis was performed in order to further evaluate the electronic state in Ni-ZCS(6%). Fig. 4(a–d) shows the XPS spectra of Zn 2p_{3/2}, Zn 2p_{1/2} (a), Cd 3d_{5/2}, Cd 3d_{3/2} (b), S 2p_{3/2}, S 2p_{1/2} (c) and Ni

2p_{1/2}, Ni 2p_{3/2} (d) respectively. The binding analysis by reference to C 1s is peaked at 284.6 eV. As can be seen from Fig. 4(a), the binding energies of 1022.7 eV and 1045.9 eV can correspond well with Zn 2p_{3/2} and Zn 2p_{1/2}. The binding energies of 405.7 eV and 412.5 eV (Fig. 4(b)) can correspond well with Cd 3d_{5/2} and Cd 3d_{3/2} respectively [51]. It can be clearly seen from the Fig. 4(a, b) that the peaks of Zn and Cd are all sharp, from which it can be determined that the valence of Zn and Cd are +2 [52]. For S 2p (Fig. 4(c)), the band can be fitted into two peaks located at 162.2 eV and 163.2 eV, respectively. The S 2p peaks of Ni-ZCS (6%) can be assigned to S 2p_{3/2} and S 2p_{1/2} [51]. Fig. 4(d) shows that the binding energies of 856.1 eV and 873.9 eV are consistent with the binding energies of Ni 2p_{3/2} and 2p_{1/2}, respectively. It can be inferred that part of S and Ni form Ni-S bond [53]. It can be seen from the Fig. 4 that the binding energy positions of Zn, Cd, S and Ni elements did not change significantly after the reaction, indicating that the catalyst maintained good stability after the reaction. In principle, researchers have found that Ni has a relatively small hydrogen adsorption heat (about 109–134 kJ/mol, Pt is 109 kJ/mol) [54]. In addition, according to the relationship between the exchange current and the bond strength of MH (M represents the transition metal) in the production of H₂, the activation energy of Ni is the lowest among all the non-noble metals and may even play a role in the hydrogen production comparable to Pt [55,56]. These concepts explain the possible role of protons Ni or their oxides in reduction reaction compared to Pt: they conduct

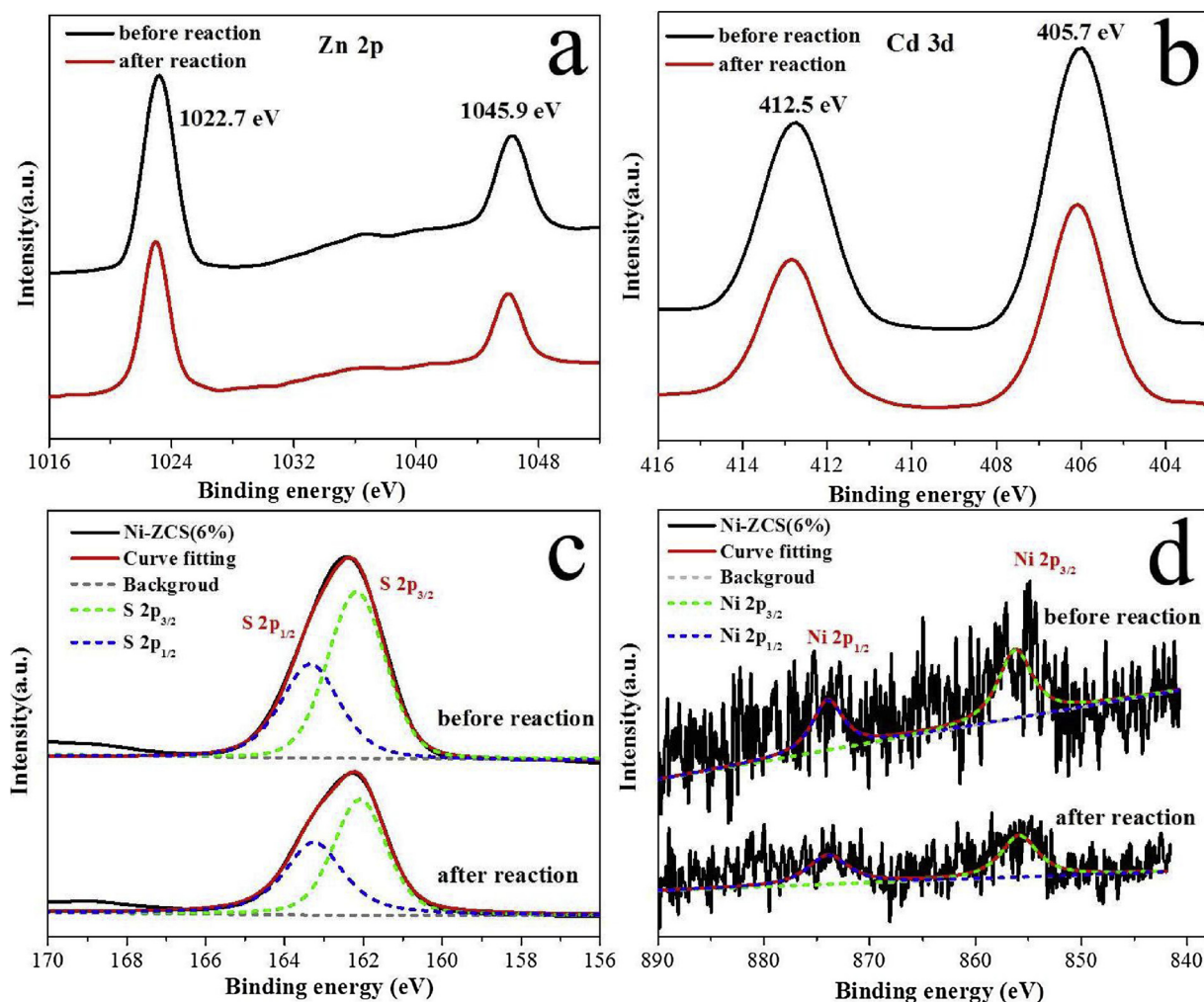


Fig. 4. High resolution XPS spectra of Zn (a), Cd (b), S (c), and Ni (d).

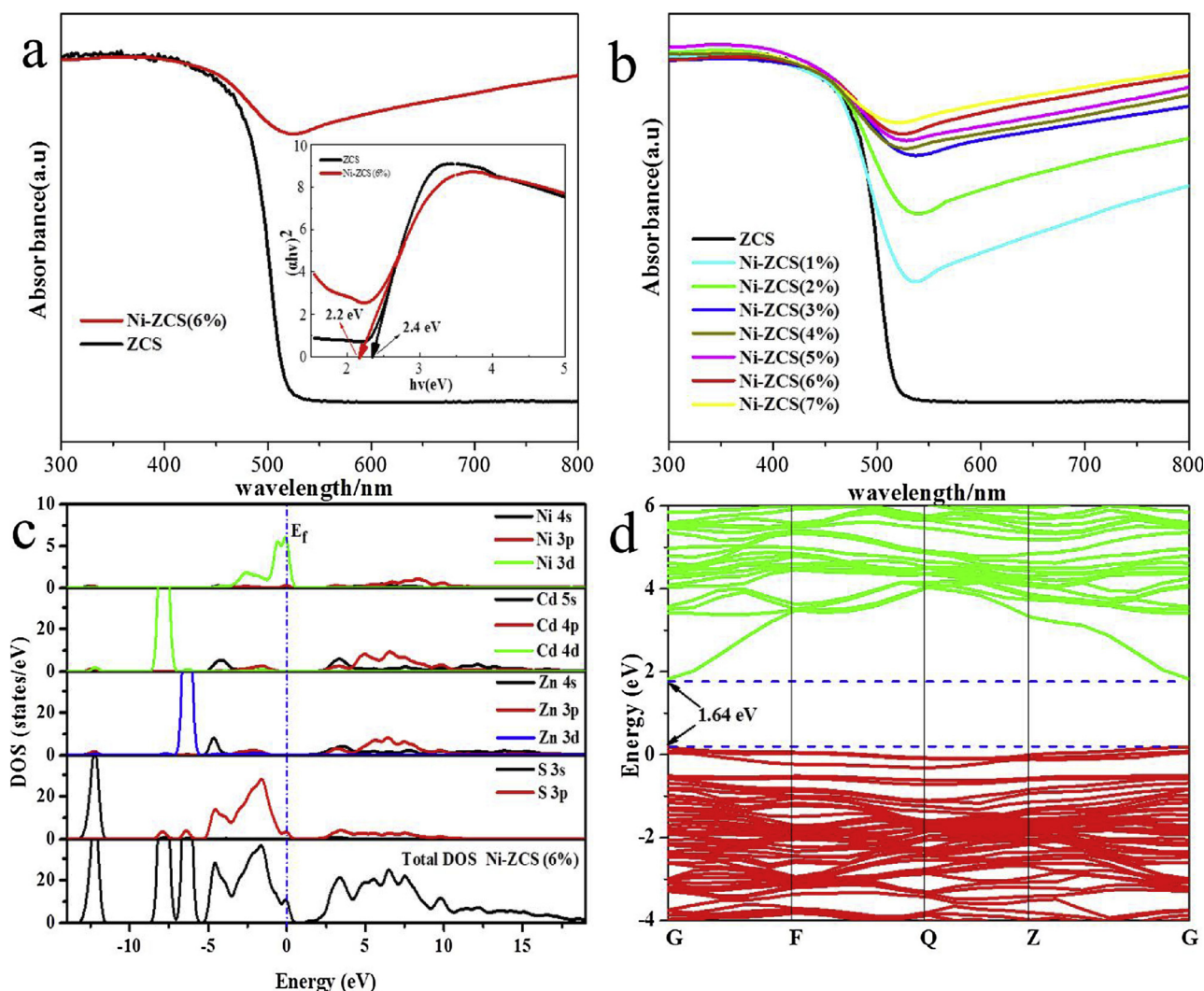


Fig. 5. (a) UV – vis absorption spectra of the ZCS and Ni-ZCS (6%), insert is the bandgaps converted from UV – vis absorption spectra; (b) UV – vis absorption spectra of the Ni-ZCS (x %), the density of states (c) and band-gap (d) of Ni-ZCS (6%).

the mass transfer process by promoting hydrogen adsorption-reduction-desorption processes.

It is necessary to explore the ability of the catalyst to respond to visible light and the effect of photocurrent-resistance on photocatalytic hydrogen production. Fig. 5(a) is the UV–vis DRS spectra of ZCS and Ni-ZCS (6%) samples. The UV–vis DRS spectra of ZCS nanoparticles indicate that an efficient absorption occurs at 490 nm, corresponding to band gap about at 2.4 eV. Compared with ZCS nanoparticles, the photocatalyst Ni-ZCS (6%) has a stronger absorption intensity which has red shifted to 510 nm, with the corresponding bandgap at about 2.2 eV, suggesting a significant change of bandgap that is owing to the introduced Ni^{2+} in the ZCS photocatalyst. Fig. 5 (b) is the UV–vis DRS spectra of Ni-ZCS (1–7%) samples, implying the UV–vis DRS spectra of Ni-ZCS(1–7%) conform well to the theoretical value.

The partial density of states (PDOS) was also calculated so that we can have an overall in-depth understanding of the band structure as well as the atomic orbital origins. The crystal structure of the Ni-ZCS is shown in Fig. S1. The total density of states (DOS) and partial density of states (PDOS) of $3 \times 3 \times 4 \text{ Zn}_{0.5}\text{Cd}_{0.5}\text{S}$ supercells are shown in Fig. 5(c). The Fermi level E_f is set at zero and indicated by vertical black dashed lines. The electronic states of valence band in the energy range between -5.37 eV and 0.6 eV are mainly ascribed to the strong S 3p states and a small number of Ni 3d electrons, and the middle valence bands in the energy range between -8.62 eV and -5.41 eV mainly come from Zn 3d

and Cd 4d states. The 3d state of Zn atoms and the 4d state of Cd atoms are very sharp, showing strong locality and no obvious interaction with other valence bands. The deep valence bands in the energy range between -13.18 eV and -11.47 eV mainly come from S 3p electrons. The electronic states of the conduction band come from the hybridization of Zn 4s, Cd 5s and S 3p states. And the valence band maximum is decided by S 3p and Ni 3d states. The band gap of Ni-ZCS (6%) is estimated to be 1.64 eV (shown in Fig. 5(d)), which is much more narrow than that of Ni-ZCS (6%) as shown in Fig. 5 (a). Usually, the band gap calculated by DFT is smaller than that by experimental results [48].

Fig. 6 (a) is the EIS Nyquist curve of ZCS and Ni-ZCS (6%), the insert presents photocurrent curve of ZCS and Ni-ZCS(6%). Compared with ZCS nanoparticles, the photocatalyst Ni-ZCS (6%) has a much smaller semicircle diameter. The insert shows that the transient photocurrent response of Ni-ZCS(6%) is about three times stronger than ZCS, demonstrating Ni-ZCS(6%) have a much lower interfacial charge-transfer resistance than ZCS in sodium sulfate buffer solution under visible light irradiation. The sharp peak of photocurrent response should be due to the accumulated charges on the surface of catalyst. In this case, the interfacial charge-carrier transfer on the surface of Ni-ZCS(6%) is faster than ZCS. The sacrificial agent Na_2S and Na_2SO_3 were employed for capturing the photo-induced holes generated on the surface of ZCS and Ni-ZCS(6%). The transient photocurrent density (Fig. 6(a), insert) directly reflects charge separation efficiency of Ni-ZCS(6%) is better than

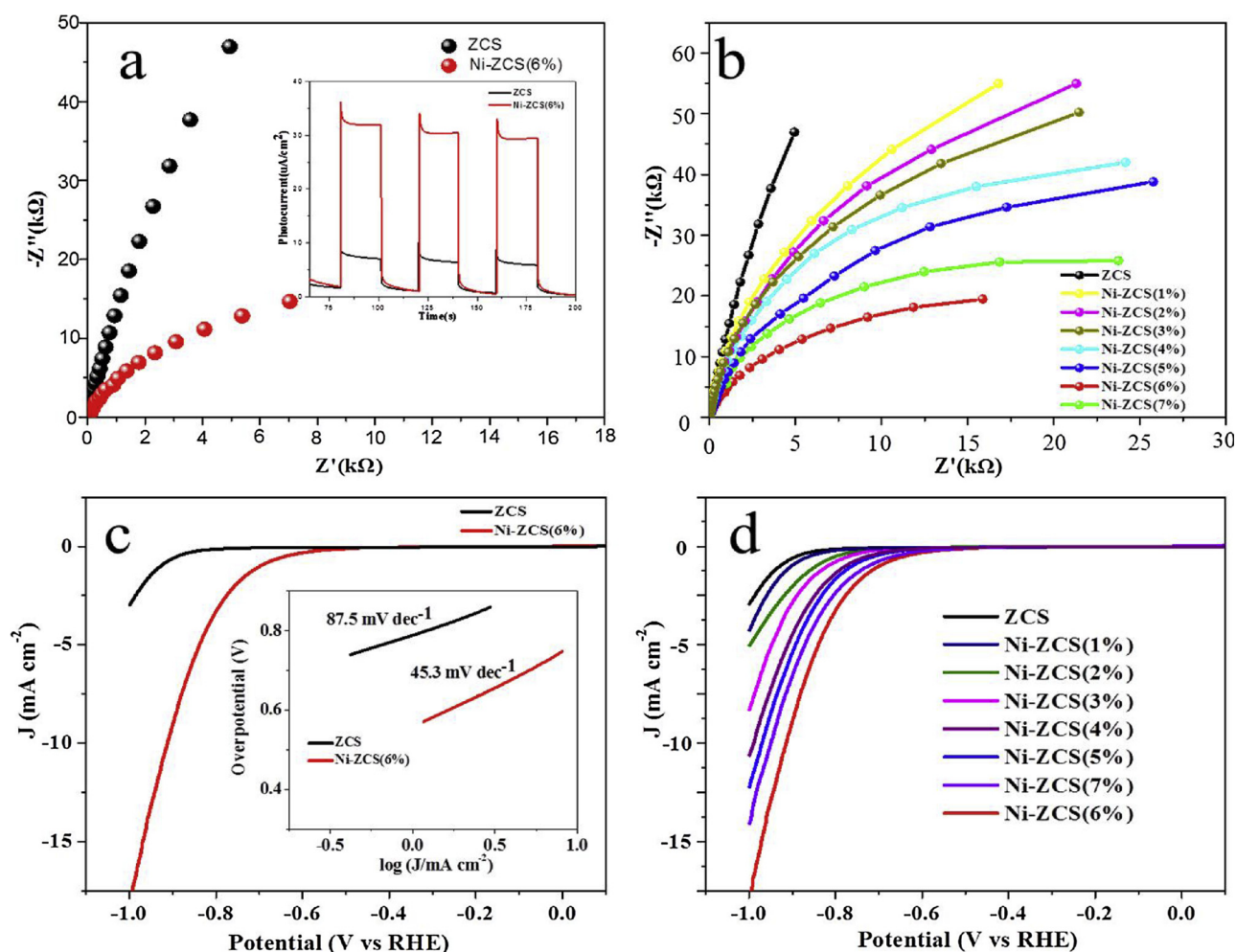


Fig. 6. (a) EIS Nyquist curves of ZCS and Ni-ZCS (6%), the inset (a) shows the photocurrent curves of ZCS and Ni-ZCS (6%) electrodes; (b) EIS Nyquist curves of Ni-ZCS (x %) electrodes measured under the open-circle potential and visible-light irradiation in 0.5 M Sodium sulfate buffer solution; (c, d) Polarization data of ZCS and Ni-ZCS (x %) electrodes, inset of c is the Tafel plots in 0.5 M Na_2SO_4 .

pure ZCS. Compared with the ZCS, with the increase in the amount of Ni doping, the samples of Ni-ZCS(x %) semicircular radius become smaller (Fig. 6(b)). when the content of the doping Ni reached to 6%, the semicircular radius was the smallest and with the lowest impedance. The above test results show that Ni-ZCS(6%) has better photoelectron and hole separation efficiency than ZCS under light irradiation. In addition, the electrochemical hydrogen evolution of ZCS and Ni-ZCS(x %) was investigated by LSV method. Fig. 6(c) and (d) shows the overpotential of different electrodes ZCS and Ni-ZCS(6%). It can be seen from the figure that the overpotential of Ni-ZCS(6%) is the lowest. The overpotential of RHE reaction has important influence on photocatalytic hydrogen production. According to the overpotential test, it can be concluded that Ni-ZCS(6%) has better photocatalytic properties. The lowest overpotential (Fig. 6(c) insert) of Ni-ZCS(6%) may be attributed to the rapid transfer of electrons, which corresponds well with the results of photocurrent and impedance experiments (Fig. 6(a, b)).

The photocatalytic H_2 evolution was tested by water splitting using a closed gas-circulation system and employing 0.5 M Na_2S and 0.5 M Na_2SO_3 as sacrificial reagents under visible light irradiation. Fig. 7(a) shows the H_2 evolution rate of these photocatalysts under visible-light irradiation. Ni-ZCS(1–7%) exhibits a higher hydrogen production performance than the pure ZCS. When the amount of doped Ni content reaches 6%, its hydrogen production rate is up to $31,000 \mu\text{mol}/\text{h}/\text{g}$, which is 6 times higher than that of pure ZCS. The quantum efficiency of Ni-ZCS(6%) is calculated to be 14.78%, which is greatly improved compared to that of the pure ZCS (Fig. S9). The stability is a very

important criterion for evaluating a catalyst. Fig. 7(b) shows the performing recycle stability experiments of Ni-ZCS(6%) in water splitting under the same conditions. It can be found that Ni-ZCS(6%) has good cycle stability while maintaining high performance. After four cycles being catalyzed by Ni-ZCS(6%), no obvious decrease can be observed in the hydrogen evolution rate, which indicates that the chemical properties of Ni-ZCS(6%) have rarely changed after a long period of photocatalytic reaction. Furthermore, the binding energy of Zn_{2p} and Cd_{3d} maintain the same value before and after the reaction. All above results suggest that Ni-ZCS(6%) catalyst is quite stable during photocatalytic reaction. The catalytic performance of Ni-ZCS(x%) in oxidation of benzyl alcohol within one hour under visible light is shown in Fig. S6. When pure ZCS is used as photocatalyst in oxidation of benzyl alcohol into benzaldehyde, yield, conversion and selectivity of the reaction are 70%, 77% and 90%, respectively. Ni-ZCS(1%) exhibits the best catalytic performance while comparing to other different amount Ni doped catalyst, 92% for the yield, 95% for the conversion, 98% for the selectivity (Fig. S6 (A)). Fig. S6 (B) shows the performance of Ni-ZCS(1%) for selective catalytic oxidation of P-nitrobenzyl alcohol, benzyl alcohol, p-methoxybenzyl alcohol and p-chlorobenzyl alcohol, respectively, all of which were conducted to generate corresponding aldehydes under visible light irradiation within 1 h. It can be seen from Fig. S6 (B) that the selective catalytic oxidation of p-nitrobenzyl alcohol is relatively low. The yield, conversion rate, selectivity of 43%, 50% and 57%, respectively, probably is caused by its relatively low solubility in BTF. Nevertheless, benzyl alcohol, p-methoxybenzyl alcohol and p-

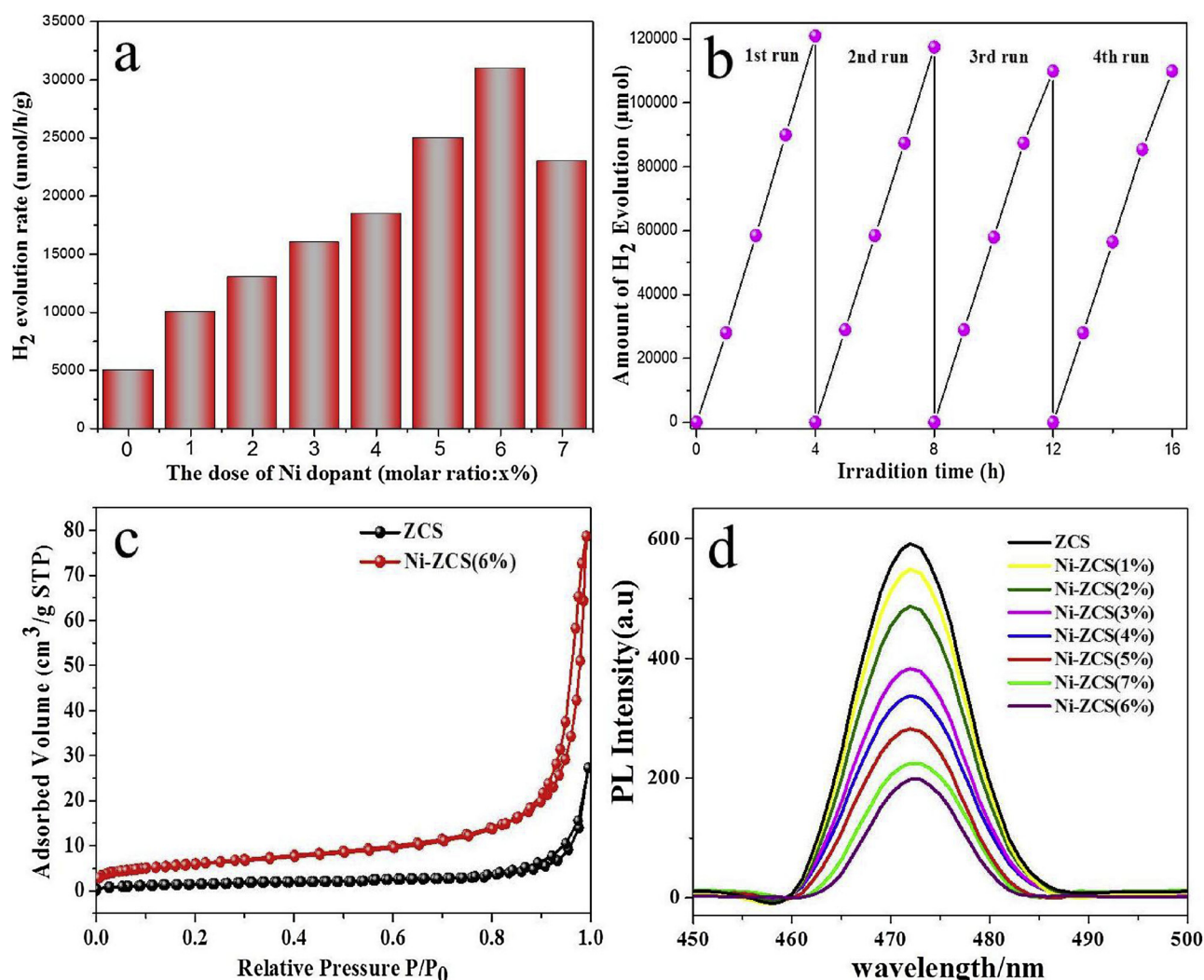


Fig. 7. (a) Photocatalytic H₂ evolution rate of ZCS and Ni-ZCS (1–7%); (b) time-cycle photocatalytic hydrogen production over Ni-ZCS (6%) with visible light illumination ($\lambda \geq 420$ nm) in 100 ml of 0.5 M Na₂S and 0.5 M Na₂SO₃ aqueous solution under visible light irradiation. (photocatalyst: 0.1 g); (c) Nitrogen adsorption-desorption isotherms curves, (d) PL spectra of ZCS and Ni-ZCS (x %) at room temperature.

chlorobenzyl alcohol show higher catalytic activity. The oxidation yield, conversion and selectivity of p-methoxybenzyl alcohol are 87%, 90% and 95%, respectively. For the oxidation of p-chlorobenzyl alcohol, the results are 90%, 92% and 95%, respectively. Since the radical $\cdot\text{O}_2^-$ and h^+ play a major role in the selective catalytic oxidation of aromatic alcohols, it can be clearly seen from Fig. 8(a, b) that the catalyst produces the radical $\cdot\text{O}_2^-$ and $\cdot\text{OH}$ in the photocatalytic process. In addition, the radical $\cdot\text{O}_2^-$ of signal peak is obviously.

Fig. 7(c) is an N₂ adsorption-desorption isotherm of ZCS and Ni-ZCS (6%) samples. It can be clearly seen from the Fig. 7(c) that the BET surface area of Ni-ZCS(6%) is larger than pure ZCS NRs, and the increased surface area can provide more active sites and enhancing photocatalytic activity. Fig. 7(d) is the photoluminescence spectra of ZCS and Ni-ZCS(x %) at the excitation wavelength of 380 nm. Photoluminescence peaks of ZCS and Ni-ZCS(x %) are situated at 472 nm and can be attributed to zinc vacancies, ZnS-associated luminescence and recombination of electrons and holes. Ni-ZCS(6%) exhibits the much weakened emission intensity than others, indicating a great decrement in the photoelectrons and holes recombination in Ni-ZCS(6%) nanocomposites, that is to say it has the best photocatalytic activity [22].

In order to further study the active groups in the photocatalytic reaction under visible light irradiation, electron-spin resonance (ESR) technique was used to detect the active groups ($\cdot\text{O}_2^-$, $\cdot\text{OH}$) of catalyst in the dark and visible light irradiation conditions using methanol and

water as solvents, respectively. As shown in Fig. 8(a), the signal of DMPO - $\cdot\text{OH}$ can be seen under visible light irradiation, and no such signal was detected in the dark. The signal peak of DMPO - O_2^- can be found in Fig. 8(b) under visible light irradiation, but no such signal is detected in the dark. Compared with the DMPO - $\cdot\text{OH}$ signal with irradiation of visible light in Fig. 8(a), the DMPO - O_2^- signal peak in Fig. 8(b) is much stronger. ESR results show that the $\cdot\text{O}_2^-$ and $\cdot\text{OH}$ radicals are produced, in addition the $\cdot\text{O}_2^-$ radicals play a major role in photocatalytic process [57,58]. This also explains the good performance of the catalyst in the reaction of selective catalytic oxidation of aromatic alcohols (Fig. S6).

To further explore the mechanism of Ni-ZCS(x %) in the photocatalytic process, it can be known from the test that the conduction band (CB) potential of Ni-ZCS(6%) is -0.34 eV RHE, and the valence band (VB) potential is 1.86 eV RHE (Fig. 8(c)) [59]. From the above test results, the photogenerated electrons in Ni-ZCS(6%) can rapidly transfer to the active sites on the surface of Ni-ZCS(6%) under light irradiation. Therefore, Ni doping can inhibit the recombination of photogenerated electrons and holes on the surface of Ni-ZCS(6%) and promote the photogenerated electrons and holes separation and transfer in Ni-ZCS(6%). Based on the above results, a possible mechanism of Ni²⁺ doping effect is proposed (Fig. 8(d)). On the one hand, Ni²⁺ partially filled d orbitals enters the lattice of ZCS, so the bandgap of nickel-doped ZCS is reduced, which is more conducive to the

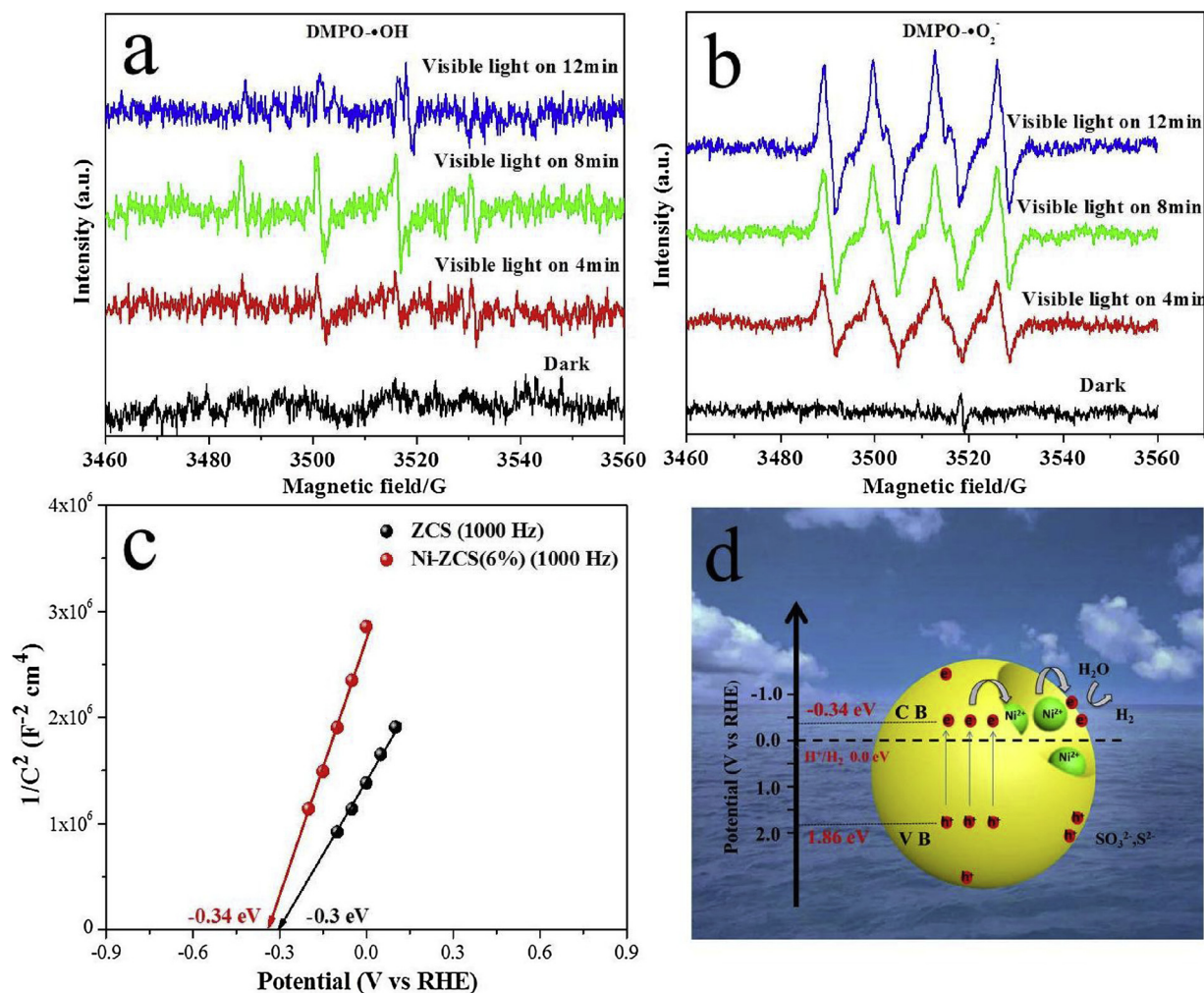


Fig. 8. ESR spectra of Ni - Zn_{0.5}Cd_{0.5}S (6%) in aqueous dispersion for DMPO - •OH (a) and in methanol dispersion for DMPO - O₂^{•-} (b) under visible light irradiation; (c) Mott-Schottky plots of ZCS, Ni-ZCS(6%) and (d) scheme of the enhanced photocatalytic H₂ evolution performance by Ni dopant ZCS.

collection of visible light and the generation of electron-hole pairs than the undoped ZCS. On the other hand, doped Ni²⁺ can act as a temporary capture site for photogenerated electrons and then transfer electrons to the catalyst surface reducing H⁺ into H₂. Simultaneously, Na₂SO₃/Na₂S solution can capture photo-induced holes and inhibit recombination of electron-hole pairs on the photocatalyst surface [60]. Hence, the separation between electrons and holes were greatly increased. The photo-induced electrons are able to further combine with O₂ to form O₂^{•-}. Both photo-induced holes and O₂^{•-} can be applied to catalyze benzyl alcohol to form benzaldehyde. The electrons can reduce H⁺ into H₂ as soon as they migrate from the inner of catalyst to the surface. Meanwhile, the substrate alcohol is oxidized into corresponding aldehyde by O₂^{•-} and holes. In this process, the separation of photo-induced charge carriers is the key step because the recombination of photo-induced electrons and holes is so quick that only a small amount of the photo-induced charges can arrive at the surface and participate in reaction. The photocatalytic activities for H₂ evolution and oxidation of aromatic alcohol will be very low if no precautions are taken to inhibit this charge recombination [36].

4. Conclusion

In summary, Ni doped ZCS have been synthesized, which can improve the photocatalytic activity under visible light irradiation. The hydrogen production rate of Ni-ZCS(6%) nanoparticle can reach 31,000 μmol/h/g, which is 6 times higher than that of the pure ZCS

with Na₂S/Na₂SO₃ as sacrificial reagents. Furthermore, selective catalytic oxidation of aromatic alcohols to generate corresponding aromatic aldehydes using Ni-ZCS(1%) as a photocatalyst has been investigated. The experiments show that the benzyl alcohol, p-methoxybenzyl alcohol and p-chlorobenzyl alcohol have the higher conversion, higher yield and higher selectivity than p-nitrobenzyl alcohol. Among them, Ni-ZCS(1%) exhibits the best catalytic performance, the yield is 92%, the conversion is 95%, the selectivity is 98%. It is confirmed that Ni-doped ZCS is not only beneficial to hydrogen production, but also has a good effect on selective catalytic oxidation. The work will provide a new strategy to design photocatalyst which can be used to catalyze the production hydrogen and selective oxidation of aromatic alcohols at the same time using visible light as a clean energy.

Acknowledgements

This work was financially supported by the National Natural Science Foundation of China (21663027, 21462039, 21808189), the Program for the Young Innovative Talents of Longyuan and the Program for Innovative Research Team (NWN-LKQN-15-2).

Appendix A. Supplementary data

Supplementary material related to this article can be found, in the online version, at doi:<https://doi.org/10.1016/j.apcatb.2019.01.002>.

References

- [1] A. Kudo, Y. Miseki, *Chem. Soc. Rev.* 38 (2009) 253–278.
- [2] A. Fujishima, K. Honda, *Nature* 238 (1972) 37–38.
- [3] L. Wu, F. Li, Y. Xu, J.W. Zhang, D. Zhang, G. Li, H. Li, *Appl. Catal. B: Environ.* 164 (2015) 217–224.
- [4] Q. Wang, J. He, Y. Shi, S. Zhang, T. Niu, H. She, Y. Bi, Z. Lei, *Appl. Catal. B: Environ.* 214 (2017) 158–167.
- [5] D. Pan, Z. Han, Y. Miao, D. Zhang, G. Li, *Appl. Catal. B: Environ.* 229 (2018) 130–138.
- [6] Y. Feng, H. Li, L. Ling, S. Yan, D. Pan, H. Ge, H. Li, Z. Bian, *Environ. Sci. Technol.* 52 (2018) 7842–7848.
- [7] G. Li, Z. Lian, W. Wang, D. Zhang, H. Li, *Nano Energy* 19 (2016) 446–454.
- [8] Q. Wang, T. Niu, L. Wang, J. Huang, H. She, *Chin. J. Catal.* 39 (2018) 613–618.
- [9] Q. Wang, N. An, W. Chen, R. Wang, F. Wang, Z. Lei, W. Shang guan, *Int. J. Hydrogen Energy* 37 (2012) 12886–12892.
- [10] L. Wang, S. Duan, P. Jin, H. She, J. Huang, Z. Lei, T. Zhang, Q. Wang, *Appl. Catal. B: Environ.* 239 (2018) 599–608.
- [11] M. Liu, D. Jing, Z. Zhou, L. Guo, *Nat. Commun.* 4 (2013) 2278–2285.
- [12] T. Zhuang, Y. Liu, M. Sun, S. Jiang, M. Zhang, X. Wang, Q. Zhang, J. Jiang, S. Yu, *Angew. Chem. Int. Ed.* 39 (2015) 11495–11500.
- [13] H. She, H. Zhou, L. Li, Z. Zhao, M. Jiang, J. Huang, L. Wang, Q. Wang, *ACS Sustain. Chem. Eng.* (2018), <https://doi.org/10.1021/acssuschemeng.8b04250>.
- [14] C. Zhang, H. Liu, W. Wang, H. Qian, S. Cheng, Y. Wang, Z. Zha, Y. Zhong, Y. Hu, *Appl. Catal. B: Environ.* 239 (2018) 309–316.
- [15] B. He, R. Liu, J. Ren, C. Tang, Y. Zhong, Y. Hu, *Langmuir* 33 (2017) 6719–6726.
- [16] H. Du, H. Guo, Y. Liu, X. Xie, K. Liang, X. Zhou, X. Wang, A. Xu, *ACS Appl. Mater. Interfaces* 8 (2016) 4023–4230.
- [17] H. Wang, Y. Li, D. Shu, X. Chen, X. Liu, X. Wang, J. Zhang, H. Wang, *Int. J. Energy Res.* 40 (2016) 1280–1286.
- [18] F. Xue, W. Fu, M. Liu, X. Wang, B. Wang, L. Guo, *Int. J. Hydrogen Energy* 41 (2016) 20455–20464.
- [19] J. Ran, J. Zhang, J. Yu, S. Qiao, *ChemSusChem* 7 (2014) 3426–3434.
- [20] Y. Yu, J. Zhang, X. Wu, W. Zhao, B. Zhang, *Angew. Chem. Int. Ed.* 51 (2012) 897–900.
- [21] F. Liu, X. Wang, J. Li, H. Wang, M. Yang, *Mater. Res. Innov.* 18 (2013) 443–450.
- [22] Q. Wang, J. Li, Y. Bai, J. Lian, H. Huang, Z. Li, Z. Lei, W. Shang guan, *Green Chem.* 16 (2014) 2728–2735.
- [23] R. Shi, H.-F. Ye, F. Liang, Z. Wang, K. Li, Y. Weng, Z. Lin, W.-F. Fu, C.-Mi. Che, Y. Chen, *Adv. Mater.* 30 (2018) 1705941–1705946.
- [24] Y. Sang, Z. Zhao, M. Zhao, P. Hao, Y. Leng, H. Liu, *Adv. Mater.* 27 (2015) 363–369.
- [25] S. Lu, B. Tong, H. Yu, I. Waterhouse, C. Geoffrey, Y. Zhou, M. Zhao, L. Tahir, C. Wu, T. Tung, Zhang, *Adv. Energy Mater.* 6 (2016) 1501241–1501248.
- [26] B. Dipankar, Z. Khan, N. Vinothkumar, M. De, Qureshi, *Indian J. Chem. A* 116 (2012) 150–156.
- [27] T. Kato, Y. Hakari, S. Ikeda, Q. Jia, A. Iwase, A. Kudo, *J. Phys. Chem. Lett.* 6 (2015) 1042–1047.
- [28] J. Zhang, J. Yu, Y. Zhang, Q. Li, J. Gong, *Nano Lett.* 11 (2011) 4774–4779.
- [29] H. Pang, C. Wei, X. Li, G. Li, Y. Ma, S. Li, J. Chen, J. Zhang, *Sci. Rep.-UK* 4 (2014) 3577–3584.
- [30] S. Shen, A. Ma, Z. Tang, Z. Han, M. Wang, Z. Wang, L. Zhi, J. Yang, *ChemCatChem* 7 (2015) 609–615.
- [31] S. Tajima, S. Kuroshima, Y. Katayama, T. Tamai, N. Sada, K. Hirai, Kenji, *Eur. J. Inorg. Chem.* 18 (2017) 2444–2449.
- [32] Y. Chen, S. Zhao, X. Wang, Q. Peng, R. Lin, Y. Wang, R. Shen, X. Cao, L. Zhang, G. Zhou, J. Li, A. Xia, Y. Li, *J. Am. Chem. Soc.* 138 (2016) 4286–4289.
- [33] E.A. Kozlova, S.V. Cherepanova, D.V. Markovskaya, A.A. Saraev, E.Y. Gerasimov, V.N. Parmon, *Appl. Catal. B: Environ.* 183 (2016) 197–205.
- [34] H. Liu, Z. Jin, Z. Xu, *Dalton Trans.* 44 (2015) 14368–14375.
- [35] D.V. Markovskaya, E.A. Kozlova, S.V. Cherepanova, A.A. Saraev, E.Y. Gerasimov, V.N. Parmon, *Top. Catal.* 59 (2016) 1297–1034.
- [36] J. Yu, J. Zhang, M. Jaroniec, *Green Chem.* 12 (2010) 1611–1615.
- [37] E.A. Kozlova, A.Y. Kurenkova, V.S. Semeykina, E.V. Parkhomchuk, S.V. Cherepanova, E.Y. Gerasimov, A.A. Saraev, V.V. Kaichev, V.N. Parmon, *ChemCatChem* 7 (2015) 4108–4117.
- [38] H. Yu, X. Huang, P. Wang, J. Yu, *J. Phys. Chem. C* 120 (2016) 3722–3730.
- [39] W. Zhang, Z. Zhong, Y. Wang, X. Rong, *J. Phys. Chem. C* 112 (2008) 17635–17642.
- [40] G. Liu, L. Zhao, L. Ma, L. Guo, *Catal. Commun.* 9 (2008) 126–130.
- [41] K. Zhang, D. Jing, Q. Chen, L. Guo, *Int. J. Hydrogen Energy* 35 (2010) 2048–2057.
- [42] Y. Yu, G. Chen, L. Hao, Y. Zhou, Y. Wang, J. Pei, J. Sun, Z. Han, *Chem. Commun.* 49 (2013) 10142–10144.
- [43] X. Zhang, D. Jing, M. Liu, L. Guo, *Catal. Commun.* 9 (2008) 1720–1724.
- [44] X. Zhang, D. Jing, L. Guo, *Int. J. Hydrogen Energy* 35 (2010) 7051–7057.
- [45] Y. Wang, J. Wu, J. Zheng, R. Jiang, R. Xu, *Catal. Sci. Technol.* 2 (2012) 581–588.
- [46] Q. Wang, J. He, Y. Shi, S. Zhang, T. Niu, H. She, Y. Bi, *Chem. Eng. J.* 326 (2017) 411–418.
- [47] Q. Wang, T. Niu, L. Wang, C. Yan, J. Huang, J. He, H. She, B. Su, Y. Bi, *Chem. Eng. J.* 337 (2018) 506–514.
- [48] J.P. Perdew, M. Levy, *Phys. Rev. Lett.* 51 (1983) 1884–1887.
- [49] J.P. Perdew, K. Burke, M. Ernzerhof, *Phys. Rev. Lett.* 77 (1996) 3865–3868.
- [50] G. Kresse, D. Joubert, *Phys. Rev. B* 59 (1999) 1758–1775.
- [51] H. Zhao, R. Sun, X. Li, X. Sun, *Mat. Sci. Semicond. Proc.* 59 (2017) 68–75.
- [52] J. Song, H. Zhao, R. Sun, X. Li, D. Sun, *Energy Environ. Sci.* 10 (2017) 225–235.
- [53] Y. Yu, E. Wang, *Dalton Trans.* 47 (2018) 1171–1178.
- [54] S. Trasatti, *J. Chem. Soc.* 68 (1972) 229–236.
- [55] J. Yang, D. Wang, H. Han, C. Li, *Acc. Chem. Res.* 46 (2013) 1900–1909.
- [56] S. Trasatti, *J. Electroanal. Chem.* 39 (1972) 163–184.
- [57] Y. Jia, S. Li, J. Gao, G. Zhu, F. Zhang, X. Shi, Y. Huang, C. Liu, *Appl. Catal. B: Environ.* 240 (2019) 241–252.
- [58] G. Zhu, M. Hojamberdiev, S. Zhang, S.T.U. Din, W. Yang, *Appl. Surf. Sci.* 467–468 (2019) 968–978.
- [59] H. Ye, R. Shi, X. Yang, W. Fu, Y. Chen, *Appl. Catal. B: Environ.* 233 (2018) 70–79.
- [60] N.S. Begum, H.M. Farveez Ahmed, K.R. Gunashekar, *Bull. Mater. Sci.* 31 (2008) 747–751.